JOURNAL OF COMPUTATIONAL PHYSICS 106, 377–390 (1993)

A Monte Carlo Code Describing the Neutral Gas Transport in Pipe Configurations with Attenuating Media

A. NICOLAI

Institut für Plasmaphysik, Forschungszentrum Jülich GmbH, Assoziation EURATOM-KFA, Postfach 1913, D-5170 Jülich, Germany

Received August 29, 1990

A three-dimensional Monte Carlo description of the neutral gas transport in pipe configurations with almost arbitrary torsion and curvature is presented. To avoid quadratic or even transcendental expressions describing the pipe surfaces confining and guiding the neutral gas, a decomposition into plane geometrical elements is chosen. Furthermore, a combination of the pseudo collision, "pseudo tracklength," and of the standard tracklength estimator is introduced. The pseudo collision estimator or—mainly for comparison—the pseudo tracklength estimator are used in the plasma domain. The standard tracklength estimator is employed in the vacuum regions to avoid the introduction of an artificially scattering medium there. This estimator combination allows us to treat the throat plasma similarly to a homogeneous absorbing medium (speeding up the geometrical and atomic physics related calculations) and to use the standard tracklength estimator if the tracklength is to be calculated during particle tracing anyway. To reduce the variances, importance sampling is applied leading to an exponential 1D-importance function. The validation of the code EOS II is based on a comparison of analytical conductances and a simple analytical solution of the neutral gas transport in a homogeneous plasma slab with the respective code results. Furthermore, the results obtained by the pseudo collision estimator are compared with those of the pseudo tracklength estimator; the equivalence of the two estimators in media with strong and weak attenuation is demonstrated. In particular it is shown that both estimators may be combined with importance sampling. Applications to the pump limiter facility ALT-II show the practical expediency of the code.

INTRODUCTION

Two-dimensional descriptions of the neutral gas transport in poloidal divertor and limiter scrape off regions and in the pumping plenum of pump limiters have been attempted already [1–4] employing Monte Carlo methods. In these approaches the confining walls have been described, as proposed in [5], by quadratic surfaces which are to be introduced piecewise by prescribing the respective set of coefficients. However, in the case of general pipe configurations which are used to guide the neutral gas flow, it might be more appropriate to choose a parametrization which is inherent to the particular geometry of the (in principle transcendental) pipe surfaces. Thus a pipe surface may be described by the length of its centerline s, the torsion $\tau(s)$ and the curvature $\kappa(s)$ of this line as proposed in standard textbooks (e.g., [6]). Hence, in this paper a procedure is presented in which the parameters s, κ, and τ are used to define the centerline of pipe surfaces of practical interest. In a second step the procedure resorts to a decomposition of the pipe surface into quadrangles and triangles. These elements, which are comparable to the two-dimensional mesh cells used in stress analysis by finite (function) elements [7], are plane; as a consequence one normal vector per element is sufficient to define the sense of the neutral gas region with respect to the confining element and to perform the backscattering calculations (Section 4.2).

Although the number of plane elements necessary to describe a given pipe surface is in general larger than the number of the more global quadratic surfaces, a vector computer scans the plane elements faster and thus tracks the particles more efficiently because the calculation is performed in vectorizable and unrollable loops (Section 2).

Since the investigated pipe structures (mainly pump limiters), occur also in other vacuum maintaining assemblies, the majority of the methods presented in this paper, in particular the procedure for the conductance calculations, can be used for quite general purposes.

As estimators, used for scoring of the macroscopic quantities during the random walk of the neutrals, the tracklength [8–11], collision [11], and the pseudo collision [1, 11] estimator have been proposed. In the case of the tracklength estimator the geometrical calculations might become cumbersome, particularly in three-dimensional analytically prescribed meshes. If the mesh is obtained numerically (e.g., the flux surfaces provided by an equilibrium code), the application of the tracklength estimator is only feasible if a simple analytical approximation of the flux surfaces is available. The geometrical calculations are alleviated considerably by applying the pseudo collision estimator [1] which can be used in both optically thick and thin regions since the macroscopic attenuation coefficient

0021-9991/93 $5.00

due to the pseudo medium can be adjusted arbitrarily. Here in EOS II the possibility is foreseen that the total density composed of the densities of the real and the pseudo medium may be larger than the maximum real density. (In [1] the total density was limited by the maximum real density.)

A combination of the pseudo collision technique and the standard tracklength estimator yields the "pseudo tracklength estimator." Although its application needs geometrical calculations similar to those of the standard tracklength estimator, the calculation can resort to a medium with constant attenuation length so that the (pseudo or real) collision points may be sampled as in the case of the pseudo collision estimator.

In the vacuum region the tracklength estimator is in general superior to the pseudo collision estimator since no artificial scattering medium needs to be introduced. In the particular case envisioned here, the tracklength is computed anyway during particle tracking (Section 2.4).

2. DECOMPOSITION OF THE WALLS MAINTAINING THE VACUUM AND DEFINING THE PLASMA GEOMETRY

As demonstrated in Section 3 the main parts of the pump limiter assembly can be decomposed into pipes with circular or rectangular cross section. Pipe surfaces with circular cross section can be generated approximately in two steps:

1. By moving a sphere along a three-dimensional curve $\mathbf{r}(s)$ with almost arbitrary curvature and torsion the exact pipe surface is described as the envelope of the neighbouring spherical surfaces (Fig. 1) [6]; s is the arc length of the curve $\mathbf{r}(s)$.

2. The center line $\mathbf{r}(s)$ is approximated by a sequence of straight lines $\Delta\mathbf{r}_j$ (Fig. 1) and the pipe surface by a corresponding sequence of prisms with the cross-sectional shape given by regular polygons. The quadrangles building up the surfaces of the prisms are the plane elements of the pipe surface.

A somewhat similar procedure is used in the case of rectangular pipes the geometry of which is less flexible than that of the circular pipes (Section 2.2) with almost arbitrary torsion angles. This geometry, however, is still adjustable enough to describe devices as ALT-II (Section 3).

The reasons for this procedure are:

1. The quadrangles, the majority of which turn out to be rectangles, can be generated in a simple and systematic way prior to the main Monte Carlo calculation. As mentioned already, the normal vectors needed for the backscattering model can be set up in a prestep rather than computing them at each collision of the particle with the wall.

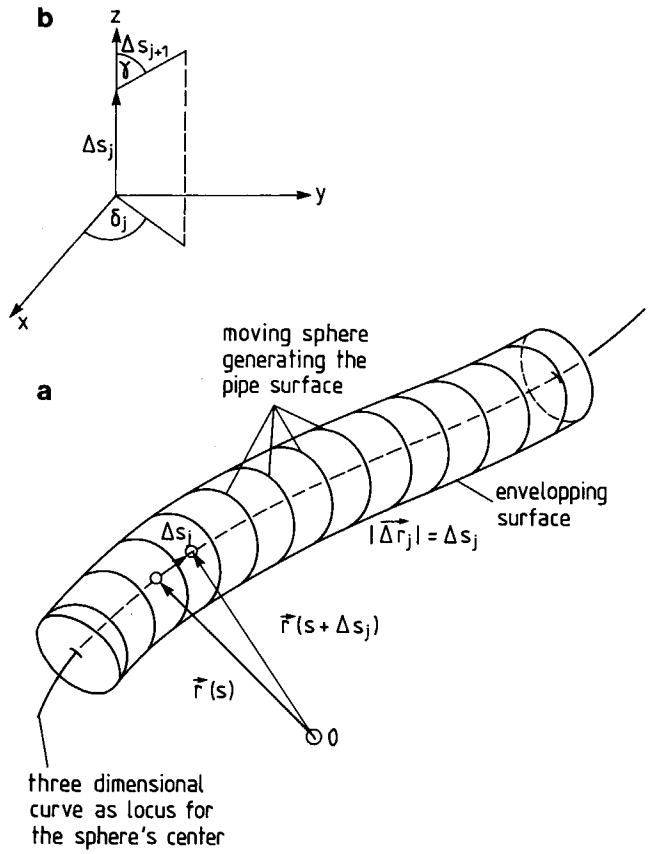

FIG. 1. A general pipe surface (a) may be generated as the envelope of a sphere moving along a prescribed 3D curve $\mathbf{r}(s)$. The $(j+1)$th pipe section is generated in the coordinate system of the jth pipe section. The axis (b) of the $(j+1)$th pipe section is defined with respect to the axis of the jth by the angle $\gamma(j)$ standing for the curvature. $\delta(j)$ is the rotation angle of the projection of the axis of the $(j+1)$th pipe into the x, y-plane of the coordinate system of the jth pipe.

2. In contrast to the quadratic surfaces [5], the coefficients of which have complicated transformation properties, the transformation of the normal vectors and of the corner coordinates can be achieved by simple rotations and translations. Furthermore, the intersection lines of the quadratic surfaces, in general described by fourth-order algebraic equations, are replaced by straight lines.

3. The intersection points of the particle path with all of the planes defined by the quadrangles can be computed in a vectorizable loop. The decision of whether or not a specific intersection point lies in a certain geometrical element is made by summing the angles swept over by the radius vector connecting the intersection point with the corners of the quadrangle. This can be included in the above-mentioned loop without impeding vectorization. In this way the number of floating point operations per microsecond achievable with a vector computer ("mega flop rate") can be increased. Specific values of the mega flop rate will be given in Section 6. The generation of the particle histories is in

general not vectorizable because many branches of this history are possible.

4. The data of the here-envisaged pipe configurations are reduced to the radii, curvature, and torsion angles, defined in the next section, whereas the quadratic surfaces need in general 10 coefficients [5] each. Moreover, the angles in the present configuration (ALT-II) [12–15]) have trivial values such as 0° or 90°.

If a pipe composed of several sections is to be moved relative to another pipe, in general six additional constants are needed for turning and shifting. However, in the case of the example given in Section 3 (ALT-II) only one set of pipes (the "scoop" pipes) is to be moved relative to another one (the "vessel" pipes).

2.1. *Circular Pipes*

To achieve a decomposition of the pipe surface, the sections $\Delta \mathbf{r}_j$ which approximate the centerline of the pipe (Fig. 1a) are described by their lengths $\Delta s_j = |\Delta \mathbf{r}_j|$ and the angles $\gamma(j)$ and $\delta(j)$ defining the direction of the section $\Delta \mathbf{r}_{j+1}$ with respect to the section $\Delta \mathbf{r}_j$ ($j = 1, ..., N_p$); N_p is the total number of circular pipes. The local coordinate system of the pipe section with index j, depicted in Fig. 1, is used. The polar angle $\gamma(j)$ stands for the curvature and is the inclination angle of the section $\Delta \mathbf{r}_{j+1}$ with respect to the section $\Delta \mathbf{r}_j$; the azimuthal angle $\delta(j)$ stands for the torsion and is the angle between the x-axis and the projection of the section $\Delta \mathbf{r}_{j+1}$ into the x, y-plane; the x-axis is perpendicular to $\Delta \mathbf{r}_j$ and is located in the plane defined by $\Delta \mathbf{r}_j$ and $\Delta \mathbf{r}_{j-1}$. Analogously, the section $\Delta \mathbf{r}_{j+2}$ is defined relative to the section $\Delta \mathbf{r}_{j+1}$ with the new x-axis lying in the plane given by $\Delta \mathbf{r}_j$ and $\Delta \mathbf{r}_{j+1}$. For $\delta(j) = 0, j = 1, 2, ..., N_p$, a pipe with a plane centerline is generated.

The pipe surface surrounding the centerline is approximated by N_p prisms with the same cross-sectional area as the real pipe. In the following mainly decagonal prisms are employed. The planes defining the surface of the prisms are generated in the local system of the respective pipe section (Fig. 1). After generating the pipe elements in the respective local systems the pipe is composed in the system of the first pipe section by transforming the coordinates of the respective prism corners into the system of the first pipe section. A change in radius is achieved by introducing frusta (truncated cones) between the pipes of different radii and by approximating these frusta by the respective frusta of pyramids.

In Fig. 2 the vacuum vessel of the advanced limiter test facility ALT-II can be seen as a specific example of a pipe with varying radius and curvature angle $\gamma(j)$.

We note that the torsion angle $\delta(j)$ must be an integral multiple of the polygonal angle $2\pi/N_r$ (N_r is the number of quadrangles building up each prism). If this condition is not fulfilled, the adjacent corners of two subsequent prisms will not coincide, giving rise to leaks on the top and the bottom of each pipe element.

2.2. *Rectangular Pipes*

Since in the case of a rectangular cross section a center of symmetry analogous to that of regular polygons is missing, only one arbitrary angle $\gamma(j)$ can be introduced; $\delta(j)$ must be an integral multiple of 90°. In this way plane pipe structures with constant rectangular cross section can be generated. Besides these plane pipes the more general case $\delta(j) = m \cdot 90°$ ($m = 0, \pm 1$) and $\gamma(j) \neq 0$ may be envisaged. However, it turns out (Section 3) that pipes with the particular choice $\delta(j) = 0$ are of major practical interest. In this case, it is possible to change the size of the rectangular cross section. Figure 2 shows the scoop ($\gamma(j) = 90°$) and the upper part of the duct of ALT-II ($\gamma(j) < 90°$) as examples. The dimension of the scoop may be characterized by the length of the deflector plate $l_d = 13.6$ cm. As in the case of the circular pipes, all pipes are generated in the respective local system and composed in the system of the first pipe.

2.3. *Advanced Geometries*

If the shape of the cross section of the pipe varies, a procedure analogous to that used with the circular pipes may still be employed if a parametric representation of the curve describing the cross section at specific values of the arc length s is available. However, in this case in general warped (twisted) quadrangles are generated; these are divided into triangles to obtain plane elements. Figure 2a shows, as an example, the wide duct between the oval port at the vacuum vessel of TEXTOR [12] and the circular port at the pumping plenum of an advanced version of an ALT-II module (more details are given in Section 3). The boundary of this pipe section is approximated by moving a straight line around the axis of symmetry of the wide duct, generating a regular surface. The decomposition into the twisted quadrangles is achieved by selecting from the straight lines making up the regular surface those which are connected to the adjacent decagonal prism.

2.4. *Mesh Cells*

To obtain a spatial resolution of the macroscopic quantities to be scored by the Monte Carlo calculation, the envisaged volumes must be subdivided into volume elements. Due to the aforementioned approximations of the pipe surfaces, the following natural volume elements are available: prisms, parallelepipeds, and frusta of pyramids. If this mesh turns out to be to coarse, the respective solids may be divided further by planes perpendicular to the centerline of the pipe. The numbering of the volume elements of the

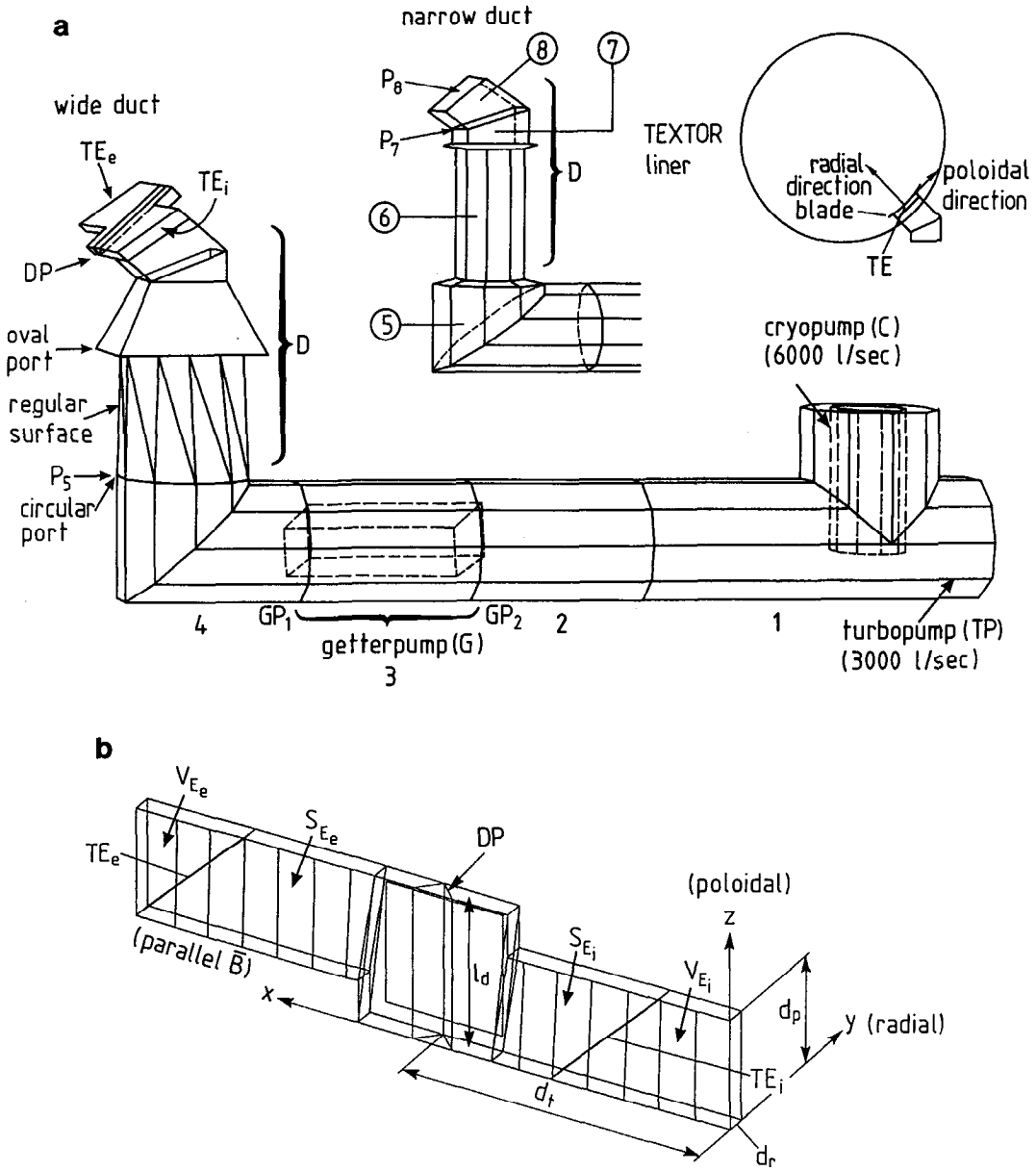

FIG. 2. The modules (a) of the pump limiter assembly ALT-II consist in general of scoops with deflector plates DP, the (circular) ducts D and the pumping plenums P which may be pumped by a getter pump G and/or a turbopump TP. In one of the modules with the (noncircular) wide duct, the cryopump can be used as an option. The deflector plates intercept via the throat entrances $TE_{e,i}$ co- and counterstreaming particles. The scoop (b) has an asymmetric shape. The central box is connected to two rectangular graphite pipes in the electron and ion drift direction. The volumes V_{E_e} and V_{E_i} are artificial; the planes defining these volumes are marked as penetrable. The modules of ALT-II are specific examples of a general pump limiter design (c). This limiter in principle consists of the pump limiter head (H) taking over the main load, the deflector plates (DP) scattering incoming ions as neutral particles preferentially into the pump duct which is connected with the pumping plenum (PP). A toroidal "blade" acts as the head in ALT-II.

vacuum vessel and the duct of ALT-II is displayed in Fig. 2a.

In the case of rectangular pipes a cartesean grid can be introduced with the axis of the coordinate system parallel to the edges of the pipe. We note that besides a zone boundary grid, a zone centered grid is used also, as in 1D-transport codes [9]. The score of EOS II is associated with the zone centered grid.

Figure 2b gives an example of the cartesean coordinate system used in the throat of ALT II. The radial, poloidal, and the parallel (to the field lines) directions are given there as well. The position of the scoop and duct relative to the liner of the tokamak TEXTOR is depicted in Fig. 2a. To achieve equal grids on the electron and on the ion sides the respective scoops, S_{E_e} and S_{E_i}, are completed by artificial volumes V_{E_e} and V_{E_i} comprising small additional parts of

the flux bundle in front of the scoop entrances TE_e and TE_i. All planes defining the artificial volumes are marked as penetrable so that in the vacuum case the configurations with and without the artificial volumes are equivalent. If the scoops with plasma are considered, the introduction of V_{E_e} and V_{E_i} means an improvement of the description since the ionization reactions outside the scoops are partly taken into account also.

Although the particles are tracked in three dimensions, no poloidal resolution is attempted since it can be assumed that the poloidal dependencies of the neutral gas parameters are small. The reason for this assumption is that both the sources and the plasma parameters have a negligible poloidal dependence as far as the throat volumes are concerned.

A lower bound on the number of the grid points in the cartesean mesh results from the maximum tolerable standard deviation in the Monte Carlo results.

3. DESIGN OF PUMP LIMITER ASSEMBLIES

A generalized pump limiter configuration is shown schematically in Fig. 2c. The pump limiter assembly consists mainly of the head (H) which absorbs most of the energy flux and a considerable part of the particle flux, both released by the central core plasma into the scrape off layer (SOL), the throat (TH) with the deflector plates (DP), the pumping duct (D), and the pumping plenum (PP). The throat has the toroidal extension d_t and the radial extension d_r. By means of the deflector plates the impinging ions are neutralized and preferentially backscattered into the pump duct, either as atoms or as molecules. Thereafter the particles may enter the pumping plenum equipped with pumps characterized by the pumping speed v_p; v_p is accounted for by an equivalent sticking probability of the pumping surface.

As a specific example, one module of ALT-II [12–15] is shown in Fig. 2a. The total assembly consists of eight modules. Each module is equipped with an octant of the blade which acts as pump limiter head, scoops with the deflector plates intercepting co- and counterstreaming particles, a duct, and a pumping plenum. Each blade octant has a toroidal extension of almost 45°; they are aligned with the inner edge at the same radius r_h. Hence the total blade acts as a toroidal limiter which is located below the equatorial plane of TEXTOR as indicated in Fig. 2a. The radial extension of the blade is 2.7 cm.

The scoop of ALT-II has an asymmetric shape and its inner surfaces are shown in more detail in Fig. 2b which depicts the decomposition into finite elements and the aforementioned cartesian grid as well. The scoop consists of a central box with deflector plates (DP) and rectangular graphite pipes in both the electron and ion drift directions.

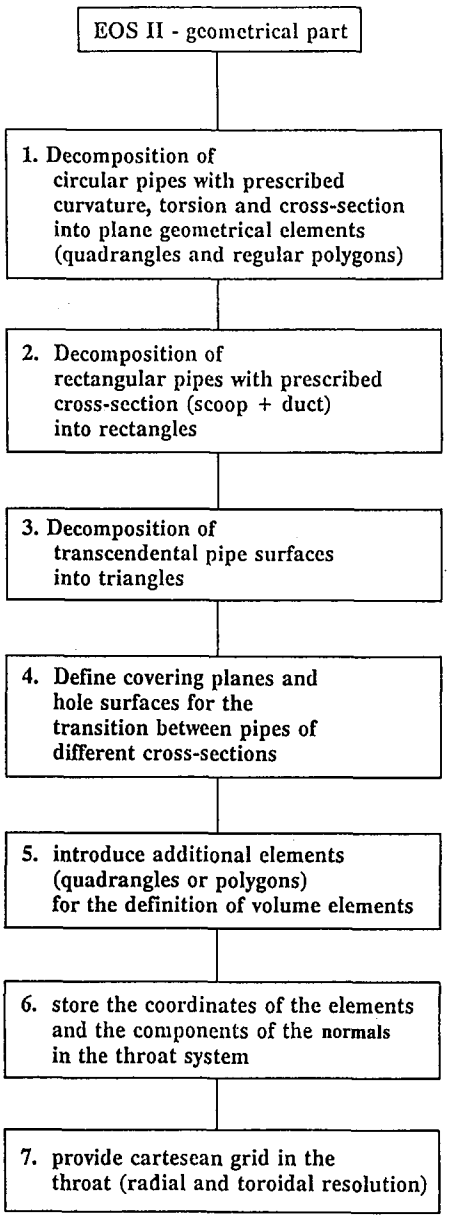

FIG. 3. The geometrical part of the code resorts to a decomposition of circular, rectangular and transcendental pipe surfaces into finite plane geometrical elements. Additional elements must be introduced to define the covering and hole planes needed for the transitions between pipes of different cross sections.

Each graphite pipe and the adjacent part of the box, together with one deflector plate, constitute one of the two throats with entrance planes TE_i and TE_e. The neutral-plasma interaction takes place in the throats; the plasma domain in the throats is divided from the vacuum region by the plane P_8 (Fig. 2a).

The pumping plenum is connected with the scoops by a duct consisting of two rectangular pipes and one cylindrical pipe in the case of the "narrow" duct (Fig. 2a). In this case the modules of ALT-II are equipped with a turbomolecular

pump which is mounted at the plane TP of the pumping plenum. Furthermore, a getter pump can be activated. This pump is located between the planes GP_1 and GP_2. The pumping speed of the turbomolecular pump is roughly $v_p = 3000$ liters/s and is simulated by an equivalent sticking probability of the plane TP. The getter consists of an array of four rectangular modules, the centerlines of which are indicated in Fig. 2a. The getter modules effect a reduction of the conductance of the pipe between GP_1 and GP_2. This reduction is accounted for by an equivalent reduction of the pipe radius between GP_1 and GP_2. The pumping speed of the getter modules ($v_p = 4000$ liters/s) is taken into account by assigning an equivalent sticking probability to the pipe wall between GP_1 and GP_2. One of the modules is equipped with the "wide" duct (Fig. 2a). Here, the pipe segment discussed in Section 2.3 is used (adjacent to the plane P5), giving rise to an improved conductance (Section 6.1). In this case, a cryopump may be activated instead of the getter pump (Fig. 2a).

Figure 3 shows a flow chart of the geometrical part of EOS-II which is applied to ALT-II. This part is mainly based on the decomposition of circular, rectangular, and transcendental pipe surfaces into finite plane geometrical elements as described in Section 2. Additional planes must be introduced to define the coverings and the holes for the transitions between pipes of different cross sections and to define the volume elements. For the backscattering model the components of the normal vectors must be stored and a cartesean grid is to be introduced in the throat.

4. MODELLING OF THE NEUTRAL GAS TRANSPORT PROCESSES BY MONTE CARLO METHODS

The performance of pump limiters is mainly determined by the plasma–neutral interaction and the backscattering of neutral particles at the walls; the treatment of these processes and the scoring of the macroscopic quantities by means of estimators is briefly described in the following, since the present application of the pseudo collision estimators is somewhat different from that in Ref. [1]. Furthermore, the definition of the pseudo tracklength estimator is based on both the pseudo collision and the tracklength estimators [11]. More details concerning the pseudo collision and standard tracklength estimators are given in, e.g., [5, 9–11, 16].

4.1. *Neutral–Plasma Interaction*

The random walk of the neutrals in an infinite plasma volume is determined by the likelihood for absorption, which may be coupled to the creation of new neutral particle species (e.g., dissociation). The influence of the walls where important sources and sink may be located is discussed later. In an inhomogeneous plasma the density function for the likelihood of a real collision is given by [5, 9–11, 16]

$$a(\mathbf{x}) = \Sigma_t(\mathbf{x}) \exp\left[-\int_0^S ds' \, \Sigma_t(\mathbf{x}(s')) \right]; \qquad (4.1.1)$$

S is the length of the particle path, $\mathbf{x}$ is the spatial vector of the particle, and $\Sigma_t(\mathbf{x})$ is the total macroscopic attenuation coefficient for the neutral particles. In the case of hydrogen atoms, this coefficient is computed from the rates for ionization, charge exchange, and multistep excitation of H_0^* ($n = 1, 2, 3$), including the transitions $1s \to 2s$, $2s \to 2p$, $2s \to 2p$, $n = 1 \to n = 2$ (total), and $n = 2 \to n = 3$ (total) [18, 19]. In the case of hydrogen molecules, $\Sigma_t(\mathbf{x})$ is obtained from the rate coefficients for molecular dissociation, molecular dissociative ionization, direct molecular ionization, molecular ion dissociative recombination, molecular ion dissociative excitation, and molecular ion dissociative ionization. These processes are described in [1, 9, 17] in more detail.

The methane-related modelling is based on the rate coefficients given in [20]. The contribution to the hydrogen deposition and density is computed from the steady-state concentrations of CH_4, CH_3, CH_2, CH, CH_4^+, CH_3^+, CH_2^+, CH^+ [18]. The helium reactions accounted for are ionization and charge exchange [1, 19].

4.2. *Backscattering*

Backscattering can be described in general by the three-dimensional distribution $\omega_{E,\theta}(E', \theta', \phi')$ dependent upon the energy E, and the polar angle θ of the incident particle, and the energy E', the polar and azimuthal angles, θ' and ϕ', of the backscattered particle [1]. The data obtained experimentally or theoretically concern the number backscattering coefficient $R_P(E)$, the energy backscattering coefficient $R_E(E)$, and the distribution ω itself [21–25]. Here it is assumed that ω may be represented in the factorized form [9]

$$\omega_{E,\theta}(E', \theta', \phi') = R_{P_1}(E, \theta) \, R_{E_1}(E, \theta, E') \, S_\theta(\theta', \phi'), \qquad (4.2.1)$$

thus renouncing the assessment of all possible distributions. The quantities R_{P_1} and R_{E_1}, both closely related to $R_P(E)$ and $R_E(E)$, may account for the results obtained by the MARLOWE code [22] or for those presented in [23].

The distribution $S_\theta(\theta', \phi')$ describes in general the transition from specular to diffuse reflection according to Ref. [1]. The cosine distribution can be used instead as an option. In particular in the case of the here-envisaged graphite deflector plates, strong erosion processes yield a rough surface favouring the assumption $S_\theta(\cos(\theta')) \sim \cos(\theta')$ [9].

Since a special backscattering model of graphite which is

dominated by porosity [26] is not available, we model backscattering at graphite walls by a reduction of the particle backscattering coefficient R_{P_1} in (4.2.1), thus accounting for enhanced sticking which leads to the release of molecules. Comparison of calculations with different reduction factors shows that the sensitivity of the results with respect to changes of R_{P_1} is small. Therefore all calculations in Sections 5 and 6 are performed with the number backscattering coefficient of Ref. [9] accounting for different target materials, e.g., carbon or iron.

4.3. *Estimators*

The scoring of macroscopic quantities (e.g., density, pressure) during the random walk of the neutrals is equivalent to solving the Boltzmann equation for the angular flux density of neutral particles [16]. Here, mainly the pseudo collision [1, 11] and the tracklength estimator [5, 8] are used. A proof of the equivalence of the two estimators is given in [27].

The pseudo collision estimator may be understood as a collision estimator used in a medium with artificially enhanced attenuation ("pseudo medium"). In [1] the maximum attenuation coefficient for the point with the minimum mean free path length is employed in the total plasma region. This procedure, however, is in general only applicable if $1/(\Sigma_t)_{\max}$ is of the order of the extension of the smallest mesh cell, so that a sufficient number of events may take place in each mesh cell. We note that this condition is only necessary and that a combination of the pseudo collision technique with importance sampling is needed to obtain a sufficiently large and roughly equal number of events in each mesh cell.

The estimators are employed to evaluate in volume V a quantity

$$E_i = \int g_i(\mathbf{x}, \mathbf{v})\, \Psi(\mathbf{x}, \mathbf{v})\, d\mathbf{x}\, d\mathbf{v} \tag{4.3.1}$$

within error limits characterized by the standard deviations inherent to the statistical method. $\mathbf{x}$ denotes a point in ordinary space and $\mathbf{v}$ a point in velocity space, where

$$\Psi(\mathbf{x}, \mathbf{v}) = |\mathbf{v}|\, f(\mathbf{x}, \mathbf{v})$$

is the angular neutral flux density and $g_i(\mathbf{x}, \mathbf{v})\,|\mathbf{v}|$ is the quantity the momentum of which is to be computed by means of the distribution function $f(\mathbf{x}, \mathbf{v})$; e.g., g_i is given by $g_i = 1/|\mathbf{v}|$ in the case of density and $g_i = \frac{1}{3}m\,|\mathbf{v}|$ in the case of scalar pressure. In a first step only real collisions are considered; the effect of the pseudo medium is discussed later. The unbiased estimator for (4.3.1) is then given by [11]

$$\eta_i(\alpha) = \sum_{m=1}^{k} e_i(\mathbf{x}_m) \tag{4.3.2}$$

for the random walk $\alpha = (\mathbf{x}_1, \mathbf{x}_2, ..., \mathbf{x}_k)$; $\mathbf{x}_1, \mathbf{x}_2, ..., \mathbf{x}_k$ are the collision points. In the case of the ionization rate, the density, and the pressure we have

$$e_1(\mathbf{x}) = Q\,\frac{\Sigma_i(\mathbf{x})}{\Sigma_t(\mathbf{x})\,V} \tag{4.3.3}$$

$$e_2(\mathbf{x}) = \frac{Q}{|\mathbf{v}|\,\Sigma_t(\mathbf{x})\,V} \tag{4.3.4}$$

and

$$e_3(\mathbf{x}) = \frac{Qm\,|\mathbf{v}|}{3\Sigma_t(\mathbf{x})\,V}, \tag{4.3.5}$$

respectively. V is the volume in which the collisions take place and Q is the source strength per second. $\Sigma_i(\mathbf{x})$ is the macroscopic attenuation coefficient due to ionization only. The contribution of a single collision in a particular volume element ΔV_j is then

$$\zeta_{i,j} = \frac{Ve_i(\mathbf{x}_m)}{\Delta V_j}\,\chi(\Delta V_j); \tag{4.3.6}$$

$\chi(\Delta V_j)$ is equal to unity if $x_n \varepsilon\, \Delta V_j$ and equal to zero otherwise. Analogous to Eq. (4.3.2), the estimator for the ionization rate, the density, and the pressure ($i = 1, 2, 3$, respectively), scored in the volume element ΔV_j, is the sum over all collision points $\mathbf{x}_m$.

If the pseudo medium is introduced, the real collision probability which distinguishes real collisions from pseudo collisions is

$$R(\mathbf{x}_i) = \frac{\Sigma_r(\mathbf{x}_i)}{\Sigma_r(\mathbf{x}_i) + \Sigma_p(\mathbf{x}_i)}; \tag{4.3.7}$$

Σ_r is the total real reaction rate. The pseudo collision rate Σ_p may be chosen such that the total reaction rate $\Sigma_t = \Sigma_r + \Sigma_p$ is constant. In this case the integrand in Eq. (4.1.1) becomes constant and sampling from the probability density (4.1.1) is greatly simplified. Here we use

$$\Sigma_t = (\Sigma_r)_{\max} \cdot \mu. \tag{4.3.8}$$

An estimate of μ is given by

$$\frac{1}{d(\Sigma_r)_{\max}} \tag{4.3.9}$$

d is the smallest extension of the mesh cells V_j. A strong variance reduction is achieved if the pseudo collision estimator [1]

$$\eta_{ps}(\alpha) = \sum_{m=1}^{k} R(\mathbf{x}_m)\, e_i(\mathbf{x}_m) \tag{4.3.10}$$

is used instead of (4.3.2). R is the above-mentioned real collision likelihood. The random walk α comprises real collisions and pseudo collision points. At the pseudo collision points the particle's weight, energy, and direction are left unchanged. At each real collision point $\mathbf{x}_i$ the weight of the particle is reduced by the factor $1-\Sigma_i(\mathbf{x}_i)/\Sigma_t(\mathbf{x}_i)$, and a new velocity is taken from a Maxwellian with the temperature of the plasma background.

The estimator (4.3.2) can be used also if a pseudo medium is superimposed. In the sum over the collision points, however, the pseudo collision points must be skipped. If the pseudo attenuation coefficient Σ_p is increased, the distances between successive pseudo collisions become shorter and the pseudo collision estimator becomes equivalent to the tracklength estimator for infinitely large Σ_p [11]. In this case the unbiased estimator for (4.3.1) reads

$$\eta_i^*(\alpha)=\sum_{m=1}^{k} e_i^*(\mathbf{x}_m, \mathbf{x}_{m+1})\, d(\mathbf{x}_m, \mathbf{x}_{m+1}); \quad (4.3.11)$$

$d(\mathbf{x}_m, \mathbf{x}_{m+1})$ is the tracklength between the collision points $\mathbf{x}_m$ and $\mathbf{x}_{m+1}$. The functions $e_i^*(\mathbf{x}, \mathbf{y})$ are given by

$$e_1^*(\mathbf{x}, \mathbf{y})=\frac{Q\Sigma_i(\mathbf{x}\to\mathbf{y})}{V} \quad (4.3.12)$$

$$e_2^*(\mathbf{x}, \mathbf{y})=\frac{Q}{|\mathbf{v}(\mathbf{x}\to\mathbf{y})|\, V} \quad (4.3.13)$$

$$e_3^*(\mathbf{x}, \mathbf{y})=\frac{Q\,|\mathbf{v}(\mathbf{x}\to\mathbf{y})|\, m}{3V} \quad (4.3.14)$$

for the ionization rate, density, and pressure, respectively. $\Sigma_i(\mathbf{x}\to\mathbf{y})$ and $\mathbf{v}(\mathbf{x}\to\mathbf{y})$ are the ionization attenuation coefficient and the speed along the path of the particle going from $\mathbf{x}$ to $\mathbf{y}$. The contribution of the path length $d(\mathbf{x}_m, \mathbf{x}_{m+1})$ to a particular volume element ΔV_j is

$$\zeta_{i,j}^*=\frac{Ve_i^*(\mathbf{x}_1^j, \mathbf{x}_2^j)}{\Delta V_j}\Delta_{m,j}; \quad (4.3.15)$$

$\Delta_{m,j}$ is the part of the tracklength $d(\mathbf{x}_m, \mathbf{x}_{m+1})$ inside the volume element ΔV_j and $\mathbf{x}_1^j$, $\mathbf{x}_2^j$ are the intersection points of the path $\mathbf{x}_m\to\mathbf{x}_{m+1}$ with the surface of the volume element ΔV_j. Analogous to Eq. (4.3.11), the estimator for the ionization rate, the density, and the pressure ($i=1, 2, 3$) scored in the volume element ΔV_j, is the sum over all tracklengths $d(\mathbf{x}_m, \mathbf{x}_{m+1})$.

We note that in (4.3.12) the simplifying assumption is introduced that $\Sigma_i(\mathbf{x}\to\mathbf{y})$ is constant along the path $\mathbf{x}\to\mathbf{y}$. If this is not the case, $e_1^*(\mathbf{x}, \mathbf{y})$ is to be replaced by [5]

$$e_1^*(\mathbf{x}, \mathbf{y})=\frac{Q}{V}\frac{\int_{\mathbf{x}}^{\mathbf{y}}\Sigma_i(s)\,ds}{d(\mathbf{x}, \mathbf{y})};$$

i.e., the respective estimator η_i^* scores the mean ionization rate in the volume V. Since the size of ΔV_j may be chosen such that the relative variation $\Delta\Sigma_i/\Sigma_i$ is small compared to unity, the average value $\langle\Sigma_i\rangle_{\Delta V_j}$ can be employed. We note that for the pseudo collision estimator the local attenuation rates are used exclusively.

Instead of scoring the contribution of the tracklength between two successive real collisions, the contributions (4.3.12)–(4.3.14) along the sections of the path between two successive pseudo collisions may be scored as well ("pseudo tracklength estimator").

Since in the statistical average the tracklengths sampled by means of the pseudo collision technique are the same as those sampled from the density (4.1.1) directly, the contributions to the score of a particular volume element is computed by means of the same expression (4.3.15).

In case of the pseudo tracklength estimator the absorbing medium can be treated as a homogeneous medium. Thus compared to the application of the tracklength estimator (in, e.g., [8]) the sampling of the collision points is alleviated considerably.

4.4. *Importance Sampling*

The main disadvantage of the distribution (4.1.1) is its roughly exponential decrease with increasing distance from the source point. This implies a high variance at large distances if a simple analog method is used. To avoid this, splitting and Russian roulette are applied [5, 8]. A generalization of this technique not depending on prescribed splitting surfaces and resorting to a general "importance function" is described, e.g., in [9]. In the slab geometry used here a simple exponential importance function (Section 5.2) is applied. This forces the tracklengths for (Monte Carlo) particles travelling away from the deflector plate to become longer than those in the simple analogue case; for the particles moving in the opposite direction the contrary holds.

The weight and the mean particle number are adjusted at a collision such that unbiased results are obtained.

The flow chart of the Monte Carlo part of the EOS II (Fig. 4) has as a central part the routine for tracking particles inside the pipe surfaces. If a (pseudo) collision takes place, the pseudo collision estimator may be applied and the contributions to the density pressure and the source terms are scored.

The tracklength between two collision points is decomposed, and the contributions to the respective mesh cells are scored if the pseudo tracklength estimator is used.

These estimators are applied in the throat region only. The score in the duct and the pumping plenum is obtained by means of the standard tracklength estimator. As in [9] importance sampling is applied at the real collision points.

In the case of a real collision the particle's weight is

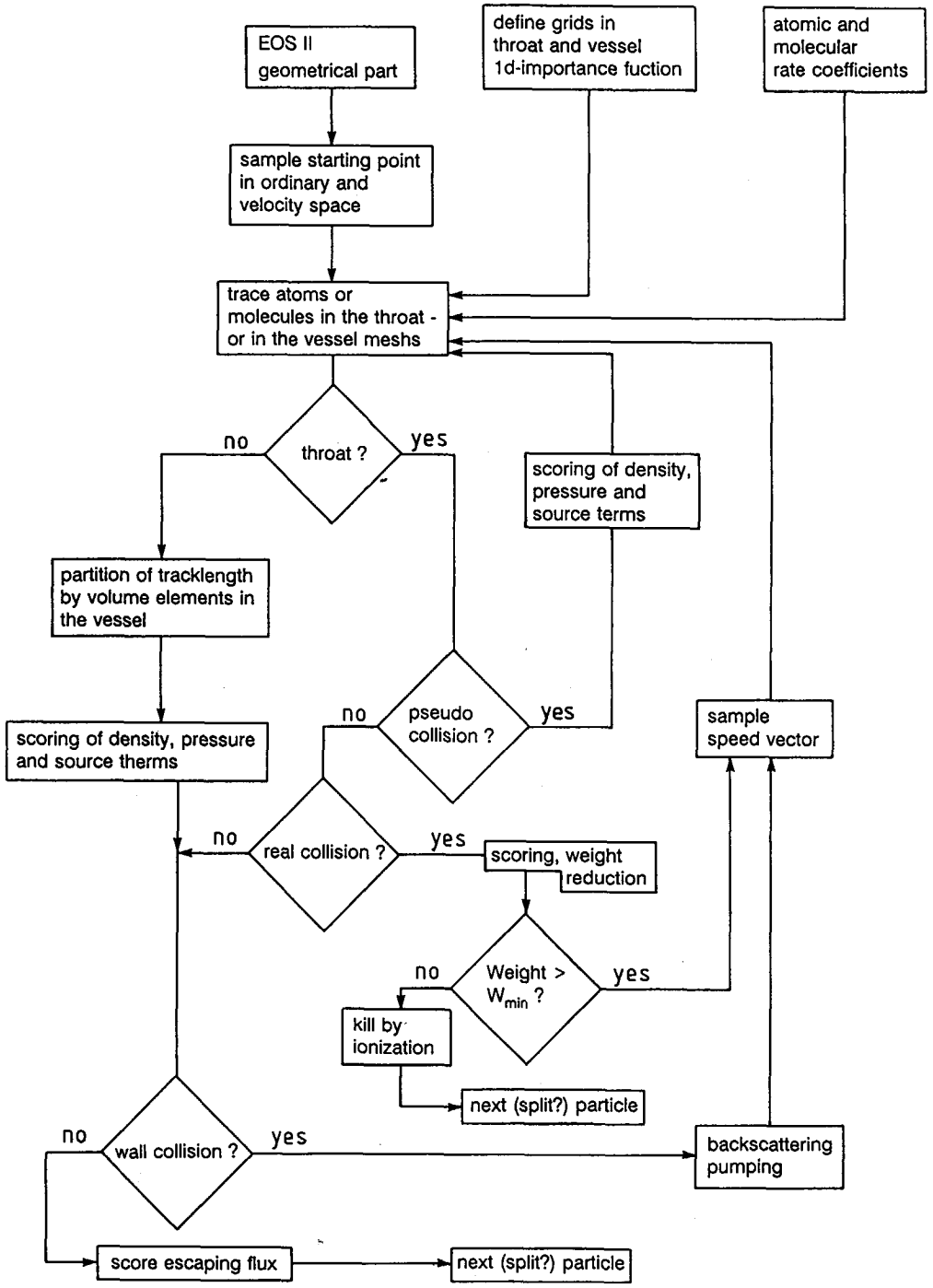

FIG. 4. The Monte Carlo part has as its central part the routine tracking particles inside the pipe surfaces. If a neutral-plasma collision takes place, the contribution to the density, pressure, and the source terms is scored. In the case of a real collision the weight of the particle is reduced. Alternatively, the contribution of the tracklength to the respective mesh cells may be scored. In the vacuum only this possibility exists.

reduced. If the weight becomes smaller than a certain limit ($10^{-4} \cdot W_0$, with W_0 as initial weight), the particle is killed by the next ionization event. In case of a collision with a confining surface element the backscattering model is applied or the escaping flux is scored. After working through all split particles the next particle is started.

For conductance calculations the hit or miss method is applied and the scoring is switched off.

4.5. *Conductance Calculations*

The conductance of a pipe structure is essentially given by the transmission probability defined by the confining walls

and two planes **a** and **b** at the upstream and downstream ends respectively [28, 29]. The transmission probability is the likelihood that a particle started at a plane **a** with a uniform distribution over **a** and a cosine distribution in velocity space, reaches **b** without returning to **a**. Thus the transmission probability may be obtained by counting the "successful" particles.

The conductance is related to the transmission probability $t_p(\mathbf{a} \to \mathbf{b})$ by [28]

$$L = \frac{62.265}{\sqrt{M}} t_p(\mathbf{a} \to \mathbf{b})\, S_a \qquad \left[\frac{l}{\text{sec}}\right] \text{(liters/s)}. \quad (4.5.1)$$

S_a is the area of the launching plate divided by cm^2 and M is the molecular mass divided by AMU $= 1.66055\ 10^{-24}$ g. An obvious consequence of Eq. (4.5.1) is

$$t_p(\mathbf{a} \to \mathbf{b}) = \frac{S_b}{S_a} t_p(\mathbf{b} \to \mathbf{a}). \quad (4.5.2)$$

This relation can be used as a consistency check.

5. CODE VALIDATION

In the following a comparison of an analytical approximation to the conductance of a cylindrical pipe [28] with the Monte Carlo solution is presented. Neutral gas flow through a plasma slab as an absorbing medium is envisioned since in this case an analytical solution is available if simplifying assumptions are introduced.

5.1. *Comparison with Analytical Conductances*

To check the Monte Carlo procedure in general and the backscattering model in particular, the transmission probabilities of straight cylinders computed by the Monte Carlo method are compared with those obtained from analytical theory [28, 29]. Table I shows the dependence of the transmission probability on the aspect ratio A, defined here as the ratio of the length to the pipe radius. The (quadratic) cylindrical surface was accounted for exactly. The Monte Carlo results, the standard deviations of which are below 10^{-3}, agree with the analytical results to within 2%. The reason for this deviation is that the analytical results themselves have an inaccuracy of up to 2% due to the approximations in [28].

To check the approximation of the cylinders by prisms, the transmission probability of a straight cylinder ($A = 10$ in Table I) is compared with that of prisms having the same cross-sectional area but different cross-sectional shapes. Table II shows that the prism with a decagonal cross section almost has the same transmission probability as the corresponding cylinder.

5.2. *Comparison with a Simple Analytical Solution Concerning the Neutral Gas Flow through a Plasma Slab*

Now we consider a plasma slab, defined essentially by an upstream and a downstream plane. A simple analytical solution is available for particles travelling through a homogeneous plasma slab. The plasma density is $n_e = 5 \times 10^{12}/\text{cm}^3$, and the electron and ion temperatures are $T_e = T_i = 20$ eV. Only ionization is taken into account. The speed vector is assumed to be the same for all particles and to be perpendicular to the upstream plane. Simple analytical considerations yield an exponential decay for the density and the deposition profile. Comparison with the Monte Carlo results shows that these results deviate from the analytical solution at most by 5% without importance sampling and by 2.5% with importance sampling. An exponential importance function depending on the distance from the upstream plate and with the e-folding length approximately equal to the mean free path length of the neutrals was employed. At high density ($n_e = 10^{13}/\text{cm}^3$) and low density ($n_e = 5 \times 10^{11}/\text{cm}^3$) similar standard deviations are obtained.

5.3. *Comparison with Results Obtained by Means of the Pseudo-Tracklength Estimator*

The comparison with the analytical profile suffers from the fact that all particle paths are straight lines per-

TABLE I

Transition Probabilities of Cylindrical Pipes with Different Aspect Ratio

A	t_p (Monte-Carlo)	t_p (Clausing)	t_p (Dushmann)
10	0.1932	0.1973	0.1962
7	0.2481	0.2537	0.2759
5	0.3119	0.3149	0.3478

Note. The Monte Carlo results are compared with the analytical results of Clausing and Dushmann.

TABLE II

Transition Probabilities of Prismatical Pipes

Cross section	t_p (Monte Carlo)
Decagon	0.1951
Octagon	0.1975
Hexagon	0.2039
Square	0.2235

Note. The approximation by decagonal prisms provides an accuracy of 1%.

pendicular to the upstream plane, since charge exchange is ignored. Here, we take charge exchange into account and compare results obtained by different estimators. The particles released at the upstream side are sampled in ordinary space from a distribution and in velocity space from a cosine distribution.

Both the pseudo tracklength estimator and the pseudo collision estimator yield neutral gas densities which agree within the order of the standard deviations. Generalized splitting and Russian roulette based on the aforementioned importance function were applied.

5.4. *Consistency Checks*

The consistency of the calculation may be checked by the particle and energy conservation of the neutral particles within each volume element of the pump limiter assembly or within larger units composed by several volume elements. Here we concentrate on the total volume of the assembly composed of the throat, the duct, and the pumping plenum. One atomic species and its corresponding (diatomic) molecular species are considered. The flux balances for the atoms and molecules read

$$\Phi_{g_a} = \Phi_{pl_a} + \Phi_{l_a} + \Phi_{p_a} + \Phi_{r_a} \tag{5.4.1}$$

and

$$\Phi_{g_m} = \Phi_{pl_m} + \Phi_{l_m} + \Phi_{p_m} + \Phi_{d_m}, \tag{5.4.2}$$

respectively. Φ_{g_a} is the source current of atoms composed of the current released at the deflector plates and the current due to dissociation of the molecules. Analogously, Φ_{g_m} is the source current of molecules composed of the current released at the deflector plates and the current due to recombination at the walls. $\Phi_{pl_{a(m)}}$ are the atomic (molecular) currents absorbed by the plasma, $\Phi_{l_{a(m)}}$ those lost at the throat entrances and $\Phi_{p_{a(m)}}$ the pumped currents. Φ_{r_a} is the atomic flux lost due to recombination at the walls, and Φ_{d_m} is the molecular flux lost by dissociation. By adding Eqs. (5.4.1) and (5.4.2), an equation may be obtained relating the ion current Φ_{in} to the deflector plate directly to the lost, pumped, and absorbed currents, $\Phi_l = \Phi_{l_a} + 2\Phi_{l_m}$, $\Phi_p = \Phi_{p_a} + 2\Phi_{p_m}$, $\Phi_a = \Phi_{pl_a} + 2\Phi_{pl_m}$, respectively,

$$\Phi_{in} = \Phi_l + \Phi_p + \Phi_{pl}. \tag{5.4.3}$$

Thus, the recombination and dissociation fluxes (which are not absorbed or pumped) are eliminated from the expressions (5.4.1) and (5.4.2).

The calculations concerning ALT-II given in the next section show that the relative deviations between the RHS and the LHS of Eqs. (5.4.1), (5.4.2), and (5.4.3) are less than 5×10^{-3}.

TABLE III

Dependence of the Mega Flop Rate MF, the Number of Tracked Particles N_p on the Number of Surfaces n_s

Cray option	n_s	s_d (%)	N_p	MF
Scalar operation	10	0.55	135200	6.1
Vector operation	20	0.42	214100	28.5
Vector operation	40	0.45	177300	43.5
Vector operation	60	0.48	150300	54.8
Vector operation	80	0.53	124500	60.3

Note. In case of vectorized operation MF saturates at around MF = 60.

6. APPLICATIONS

These calculations consider the evaluation of conductances and neutral gas parameters in the throat and the pumping plenum of ALT-II. For the computations an IBM 3090 computer interacting with an MVS (multiple virtual storage) batch system and a CRAY X-MP computer interacting with a UNICOS 5 batch system were employed.

6.1. *Conductances of Pipes with Constant Curvature and Torsion*

As pointed out in Section 2 a general pipe structure may be characterized by the arc length, the curvature κ, and the torsion τ of the centerline. Here we envisage pipes with constant curvature and torsion, i.e., helical pipes. The working gas is deuterium.

The calculations show, that the conductance is almost independent of the torsion. If the curvature of a pipe with length $l_p = 100$ cm and radius $r_p = 25$ cm varies from $\kappa = 0.2\ \mathrm{m}^{-1}$ to $\kappa = 0.4\ \mathrm{m}^{-1}$, the transmission probability decreases by 15%. This is much larger than the standard deviation of 1%.

The numerical advantage due to vectorized algorithms in the case of plane geometrical elements is demonstrated in Table III. A cylindrical pipe ($l_p = 100$ cm and $r_p = 10$ cm) was decomposed into $n_s = N_r N_a$ plane geometrical elements

TABLE IV

ALT-II Related Conductances

$L(\mathbf{a} \to \mathbf{b})$ (liters/s)	t_p	**a**	**b**
739	0.1770	*DP*	*TP*
546	0.1310	*DP*	TE_i, TE_e
500	0.0719	P_7	TE_i, TE_e
341	0.0218	*TP*	TE_i, TE_e
352	0.1140	TE_i, TE_e	*TP*

Note. The conductance between the deflector plates and the scoop entrances is 26% smaller than that between the deflector plates and turbopump.

(N_r is defined in Section 2.1 and N_a is the number of subdivisions on axis). In the case of 10 elements (first row of Table III) the conductance was computed by scalar operations exclusively. The mega flop rate, defined in Section 2, is MF = 6.1.

In all other cases the calculations were based on vector operations. The mega flop rate increases monotonically until the maximum value 60.3 is reached.

The number of Monte Carlo particles processed on the CRAY during a constant CPU time decreases from 214,100 to 124,500 as n_s increases from 20 to 80, and the standard deviation s_d of the transmission probability increases accordingly. The conductance obtained in the case of $n_s = 20$ is $L = 1900$ liters/s.

The table shows that the scalar calculation with 10 elements is equivalent to the analogous vector calculations for 80 elements, because they arrive at approximately the same standard deviation of the transmission probability. Since the complicated quadratic surfaces can only be treated by scalar operations which are even more time consuming than in the case of planes, these results show the improvement of the computational speed due to vectorization.

6.2. *ALT-II Related Conductances*

These calculations were based on ALT-II data (Fig. 2). The working gas is deuterium. Table IV summarizes the ALT-II related conductances and transmission probabilities; the maximum standard deviation of these quantities is below 3%. The meaning of the symbols denoting the planes **a** for launching the particles and the target plane **b** is given in Fig. 2a. The table shows that the transmission probability from the deflector plates to the throat entrances is only 26% smaller than that from the deflector plates to the turbo pump, thus showing the efficacy of the scoops. The conductance $L(TP \rightarrow TE_i, TE_e)$ between the turbo pump and the throat entrances was computed as well and checked with the conductance $L(TE_i, TE_e \rightarrow TP)$. Although the transmission probabilities differ strongly, the conductances agree within the margin of the standard deviation.

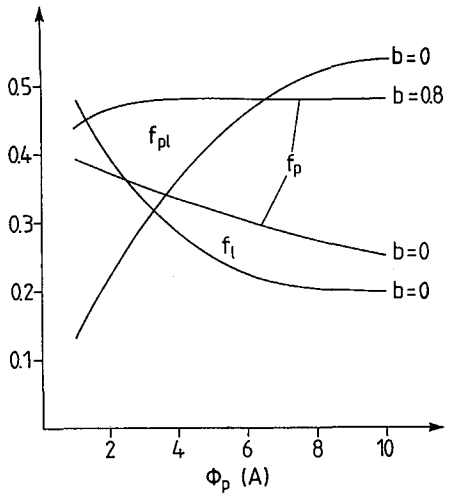

FIG. 5. The fraction f_{pl} absorbed by the plasma increases, the fraction f_l escaping via the throat entrances decreases and the pumped fraction f_p decreases as well (slowly, however) with increasing collected plasma current Φ_p (backstreaming ratio $b = 0$). For $b = 0.8$, f_p increases with increasing Φ_p.

Consequences of the conductances in Table IV are the effective pumping speeds [29] of the turbopump and the throat entrances (simulated by a sticking probability $p_s = 1$ at the entrance planes) at the deflector plates; they are 600 and 470 liters/s, respectively. These results show that particles starting at the deflector plates are preferentially pumped rather than lost.

The conductance $L(P_7 \rightarrow TE_i, TE_e)$ is 10% larger than the experimental one. This discrepancy might be due to probes in the throat which reduce the available cross section.

6.3. *Particle Removal Rate and Neutral Gas Parameters in ALT-II*

The configurations depicted in Figs. 2a and b of the 3D-geometry of ALT-II are used in the following. The results are mainly for ALT-II with narrow duct and turbo pump, since experimental data are available only for this case.

To account for the experimentally observed [13] significantly different radial decay lengths of the plasma density in the electron and ion side scoops, we assume $\lambda_e = 2$ cm and $\lambda_i = 1.5$ cm. Thus, the densities are $n_{e,i} = n_{0_{e,i}} \exp(-r/\lambda_{e,i})$; $n_{0_{e,i}}$ are the maximum densities. The electron and ion temperatures in both scoops are assumed to be $T_e = T_i = 10$ eV.

The starting points of the emerging atoms or molecules are sampled from a two-dimensional distribution along the deflector plates, the radial dependence of which is given by the ion flux density [13] $\Gamma_{e,i} = 0.5 n_{e,i} v_s$ computed from the plasma parameters. $v_s \simeq \sqrt{(T_e + T_i)/m_i}$ is approximately the ion sound speed. Here, m_i is the ion mass. The currents collected in the electron and ion side scoops are $\Phi_{e,i} = e_0 \int_0^{d_r} \Gamma_{e,i}\, dr$; d_r is the radial extension of the scoop; e_0 is the elementary charge; as a consequence the collected currents are given in amperes. The total collected flux is $\Phi_{in} = \Phi_e + \Phi_i$. A uniform distribution is assumed in the poloidal direction. The species index and the energy of the released particles are sampled according to the backscattering model of Section 4.2. The parameters of this model are as in Ref. [23]. The polar angle is sampled from a cosine distribution. As indicated by the experimental results, $\Phi_e = \Phi_i$ is assumed in the following.

Concomitant with the assessment of the particle removal rate, the neutral pressure distribution in the vacum vessel,

the neutral gas parameters, and the ion source rate in the throat are computed. The dependence of the pumped fraction (removal efficiency) $f_p = \Phi_p/\Phi_{in}$, the fraction absorbed by the plasma $f_{pl} = \Phi_{pl}/\Phi_{in}$ and the fraction lost at the throat entrances, $f_l = \Phi_l/\Phi_{in}$, on the total collected ion current Φ_{in} is given in Fig. 5. The figure shows that the

At $\Phi_{in} = 10$ A about one-half of the collected current is absorbed by the plasma and the other half is pumped or lost at the throat entrances in almost equal parts. The fraction absorbed by the plasma may stream backward to the deflector plates thus giving rise to a "vortex" flux inside the plasma circling between the plasma and the deflector plates. The curve marked by $b = 0.8$ is the pumped fraction computed by the simple approach in [14]; b is the backstreaming ratio. The fraction f_p ($b = 0.8$) increases slowly with increasing Φ_p. This trend is compatible with the experimental results.

The following results belong to the case with $\Phi_p = 10$ A. Figure 6 shows the deposition distribution H (proportional to the plasma source distribution and normalized such that its mean value is the deposited fraction) due to the molecular reactions in the throat volume. Toroidal and radial resolution is chosen because the poloidal dependence can be expected to be negligible. The distribution has a pronounced peak at $y = 0.21$ cm, $x = 30.85$ cm ($\simeq d_t$) because along this line both the flux density of the released particles and the plasma density have their maxima. (We note that the aforementioned point belongs to the zone centered grid (Section 2.4), whereas $y = 0$, $x = d_t$ belongs to the zone boundary grid.) The deposition distribution due to the atoms reveals an analogous behaviour. The deposited deuteron current is only 40% of that due to the molecular

In Fig. 7 the molecular density n_{D_2} is displayed. The maximum is at the same toroidal position as in the case of the deposition profiles. The radial dependence, however, is much weaker. The reason is the relation $n_{D_2} \sim H/(\langle \sigma v \rangle n_e)$ with the rate coefficient $\langle \sigma v \rangle$; so, the decrease of the deposition profile is compensated by the decrease in the electron density.

The maximum molecular pressure in the pipe is $p_{D_2} = 0.26$ mtorr; it is reached in the pipe element with the index $i = 7$ (Fig. 2a). The pressure decreases to $p_{D_2} = 0.075$ mtorr in the pipe element with $i = 1$ where the pump is attached. This pressure corresponds to a removal efficiency of around 25%.

f_p increases to 0.37 if the narrow duct (Fig. 2a) is replaced by the wide duct because the conductance $L(\mathrm{DP} \rightarrow \mathrm{TP}) =$ 740 liters/s rises by 30%. The closely related conductance $L(\mathrm{DP} \rightarrow \mathrm{P5})$ increases from 1100 liters/s in case of the narrow duct to 1550 liters/s in case of the wide duct. If in addition to the turbopump the cryopump with the pumping speed $v_{cr} = 6000$ liters/s is used, f_p becomes $f_p = 0.45$.

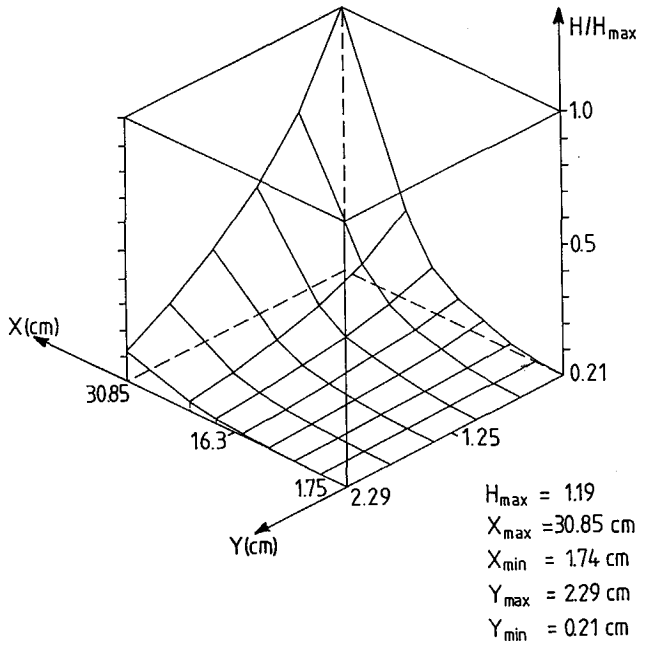

FIG. 6. Deuterons due to absorption of molecules are preferentially deposited in the vicinity of the deflector plate at smaller radii because both the flux density of released molecules and the plasma density have their maxima there.

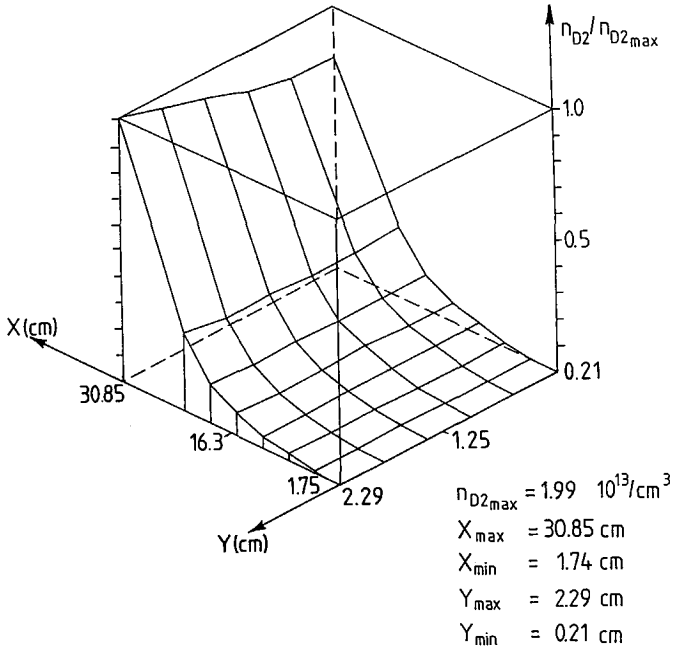

FIG. 7. The density distribution of the molecules peaks at the plates as well; the radial dependence, however, is much weaker than that of the deposition distribution in Fig. 6 because of the radial decay of the electron density.

CONCLUDING REMARKS

The results demonstrate that the geometrical part of the EOS-II code provides the ability to describe the structure of vacuum maintaining assemblies which in practice preferentially resort to pipe configurations, in a simple and straightforward way. In particular the decomposition of the pipe configurations into plane geometrical elements adapts the calculation to a vector computer, increasing the computational speed considerably.

The estimators are adjusted to the specific regions envisioned. In the vacuum region the standard tracklength estimator is used; it is particularly well-suited to mesh cells resulting from the decomposition of the pipe configurations into plane geometrical elements. In the plasma region, the pseudo collision estimator or the pseudo tracklength estimator is employed; both resort to a medium with constant attenuation length in spite of the spatially dependent plasma parameters. Although the scoring techniques of the latter estimators are quite different, the results agree well for cartesean grids. This applies to both optically thick and optically thin media.

Whereas the application of the pseudo collision estimator may be easily extended to numerically prescribed meshes, that of the pseudo tracklength estimator is restricted in the present approach to cartesean grids but may be extended to grids based on polar coordinates as well.

ACKNOWLEDGMENTS

The author thanks K. H. Finken for providing the ALT-II data, H. Kever for helpful discussions, Mrs. Hoffmann for deciphering and typing the manuscript and Mrs. Heinen for the drawings. The impetus to draft this paper was partly due to the availability of the expedient pseudo collision technique mainly presented in Ref. [1]. This is gratefully acknowledged.

REFERENCES

1. D. B. Heifetz, D. Post, M. Petravic, J. Weisheit, and G. Bateman, *J. Comput. Phys.* **46**, 309 (1982).
2. D. B. Heifetz, M. Petravic, D. E. Post, and S. Lieberson-Heifetz, *J. Nucl. Mater.* **121**, 189 (1984).
3. W. Schneider, D. B. Heifetz, K. Lackner, J. Neuhauser, D. E. Post, and K. G. Rauh, *J. Nucl. Mater.* **121**, 178 (1984).
4. D. Reiter and A. Nicolai, *J. Nucl. Mater.* **128–129**, 458 (1984).
5. L. L. Carter and E. D. Cashwell, in *Particle-Transport Simulation with the Monte Carlo Method* (Technical Information Center, Office of Public Affairs, U.S. Energy Research and Development Administration, Washington, DC, 1975), p. 44.
6. E. Kreyszig, *Introduction to Differential Geometry and Riemannian Geometry* (University of Toronto Press, Toronto, Canada, 1968).
7. O. C. Zienciewicz, *The Finite Element Method in Engineering Science*, 2nd ed. (McGraw–Hill, New York, 1971).
8. M. H. Hughes and D. E. Post, *J. Comput. Phys.* **28**, 43 (1978).
9. A. Nicolai and D. Reiter, *J. Comput. Phys.* **55**, 129 (1084).
10. D. Reiter, *Ber. Kernforsch. Jülich* **1947** (1984).
11. J. Spanier and E. M. Gelbard, *Monte Carlo Principles and Neutron Transport Problems* (Addison–Wesley, Reading/Menlo Park/London/Don Mills, 1969).
12. TEXTOR Team, Kernforschungsanlage Jülich, Institut für Plasmaphysik, Report on the Planning of TEXTOR, 1975 (unpublished).
13. R. W. Conn, S. P. Grotz, A. K. Prinja, W. B. Gauster, M. E. Malinowski, A. E. Pontau, R. S. Blewer, J. B. Witley, K. H. Dippel, and G. Fuchs, in *Proceedings, 12th Symposium of Fusion Technology, Kernforschungsanlage Jülich, Sept. 1982.*
14. W. J. Corbett, Ph.D. thesis, University of California, Los Angeles, 1989.
15. D. M. Goebel, R. W. Conn, W. J. Corbett, and K. H. Dippel, *J. Nucl. Mater.* **162–164**, 115 (1989).
16. J. M. Hammersley and D. C. Handscomb, *Monte Carlo Methods* (Chapman & Hall, London, 1979).
17. R. D. Bengtson, in *Proceedings, Conference Concerning Diagnostics for Fusion Experiments, Vienna, Austria, 1978* (Pergamon, New York, 1979).
18. J. T. Hogan, C. C. Klepper, D. L. Hillis, and T. Uckan, *J. Nucl. Mater.* **162–164**, 469 (1989).
19. K. Janev, W. D. Langer, K. Evans, and D. Post, *Atomic and Molecular Processes in Hydrogen–Helium Plasmas* (Springer-Verlag, Hamburg, in press).
20. A. B. Ehrhardt and W. D. Langer, Princeton Plasma Physics Laboratory Report PPPL-2477, 1987 (unpublished).
21. T. Tabata, R. Ito, Y. Itikawa, N. Itoh, and K. Morita, Institute of Plasma Physics, Nagoya University Report IPPJ-AM-18, 1981 (unpublished).
22. O. S. Oen and M. T. Robinson, *J. Nucl. Mater.* **76/77**, 370 (1978).
23. R. Behrisch, in *Proceedings, Summer School of Tokamak Reactors for Breakeven, Erice, 1976* (unpublished).
24. M. T. Robinson and I. M. Torrens, *Phys. Rev. B* **9**, 5008 (1974).
25. W. Eckstein and H. Verbeck, Max-Planck Institut für Plasmaphysik Report IPP 9/32, 1979 (unpublished).
26. T. Kiyoshi, T. Namba, and M. Yamawaki, "Hydrogen Permeation through Graphite," Proceedings, Int. Conf. on Fusion React. Mater., Karlsruhe, West Germany, 1987.
27. G. G. Lister, D. E. Post, and R. J. Goldston, in *Proceedings, 3rd Symposium on Plasma Heating in Toroidal Devices, Bologna, Italy, 1976*, p. 303.
28. P. Clausing, *Ann. Phys.* **5**, (12), 961 (1932).
29. S. Dushmann, *Scientific Foundations of Vacuum Technique* (Wiley, New York, 1972).